COMPOSITION OF PLASMAS FORMED FROM DEBRIS IMPACTS ON SPACECRAFT SURFACES

Nicolas Lee*[(1)], Sigrid Close[(1)], and Ralf Srama[(2)]

[(1)]*Department of Aeronautics and Astronautics, Stanford University, Stanford, CA, 94305, USA*
[(2)]*Institut für Raumfahrtsysteme, Universität Stuttgart, Pfaffenwaldring 29, 70569 Stuttgart, Germany*

ABSTRACT

The threat of electrical anomalies caused by plasma resulting from hypervelocity impacts of meteoroids and space debris has thus far not been well characterised. Here we present results from a ground-based hypervelocity impact experiment with measurements of the impact plasma formed by iron projectiles impacting on representative spacecraft materials at speeds characteristic of both meteoroids and space debris. These experiments were conducted using a Van de Graaff dust accelerator with projectiles ranging from 10^{-16} to 10^{-11} g in mass. We find that a mixture of negative ion species are produced and ejected from negatively-biased impact surfaces, and that the dependence of electron production on impact speed is weaker for surfaces with a conductive coating.

Key words: Hypervelocity impact; space plasma; electrical anomalies.

1. INTRODUCTION

The space debris population in Earth orbit is composed of many objects that are too small to be tracked and avoided. Accordingly, the threat posed by these small objects can only be mitigated through proper shielding of sensitive spacecraft systems. In low Earth orbit (LEO), the average impact speed between debris objects and spacecraft is approximately 10 km/s [1], while meteoroids can impact spacecraft at speeds of over 70 km/s [2]. In geosynchronous Earth orbit (GEO), the threat of debris impacts is reduced because of lower relative speeds and lower number densities. These impacts pose a threat not only of mechanical damage but also of electrical damage. Upon impact, a small, dense plasma is formed as the kinetic energy of the impactor is rapidly converted in part to energy of vaporisation and ionisation. The charged constituents of the plasma rapidly expand and can result in electrical anomalies within the spacecraft. These anomalies may result from an electromagnetic pulse radiating from the expanding plasma [3], an electrostatic discharge or arcing event triggered by the impact, or a combination of multiple effects.

In order to protect spacecraft electrically from these effects, a shielding mechanism can be targeted at affecting the impact phenomenon by reducing the charge produced or disrupting the plasma expansion, or it can be targeted at preventing any electrical effect from penetrating into spacecraft electronics. Accomplishing either function requires that the properties of the hypervelocity impact plasma are understood. In 2011, we conducted experiments using the Van de Graaff dust accelerator at the Max Planck Institute for Nuclear Physics (MPIK) in Heidelberg, Germany, to study the formation and behaviour of impact plasmas from iron projectiles impacting a variety of representative spacecraft materials under a range of surface charging conditions. These impacts were observed using plasma, optical, and radio frequency (RF) sensors.

In this paper, we present an analysis of the plasma measurements from impacts on five different spacecraft materials. We find that the composition of the plasma exhibits a strong dependence on the target material and that the dependence on impact speed also varies with target material. In section 2, we describe the experiment configuration, including the sensors and targets used. We then present the analysis of plasma measurements in section 3. Finally, we conclude with a discussion of implications for spacecraft design and of possible future work in section 4.

2. EXPERIMENT

The Van de Graaff dust accelerator uses a 2 MV electrostatic terminal to accelerate positively charged iron spheres along a drift tube and into a test vacuum chamber. Mocker et al. [4] provide a detailed description of the facility. Impacts of iron projectiles ranging in mass from 0.1 fg (1×10^{-16} g) to 10 pg (1×10^{-11} g) at speeds between 3 and 66 km/s were observed, spanning typical impact speeds of space debris as well as meteoroids. Impact surfaces representative of spacecraft materials, including solar cells, optical solar reflectors (OSRs), and

*Now at Division of Engineering and Applied Science, California Institute of Technology, Pasadena, CA, 91125, USA

a solar panel substrate, were used in addition to metallic surfaces. These impact surfaces were biased through a current-controlled voltage supply to represent spacecraft charging effects. The impacts occurred in a vacuum ranging from 3×10^{-6} to 1×10^{-5} mbar, corresponding to a mean free path greater than the chamber diameter of 1.4 m and allowing for free (collisionless) expansion of the impact plasma.

2.1. Experimental Configuration

The impacts were observed by a pair of retarding potential analysers (RPAs) to measure the plasma current, six patch antennas to measure electromagnetic RF emission associated with the impact, and a photomultiplier tube (PMT) to measure the impact-produced optical flash. The sensors and the targets were arranged as shown in Fig. 1. The targets were oriented at an angle of 30° from vertical. The RPAs were positioned 65 and 85 mm from the point of impact at approximately ±30° azimuth. The PMT was positioned between the RPAs at a range of 110 mm and at 50° elevation. The six patch antennas were tuned for response at 315 and 916 MHz and were positioned 120 to 220 mm from the impact point.

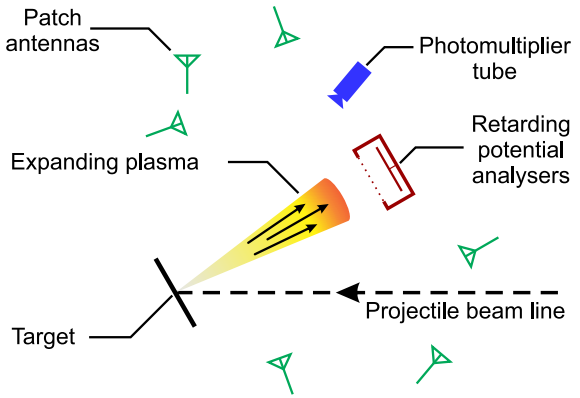

Figure 1. Side view schematic representation of the test chamber with sensors and targets. The accelerator fires projectiles from right to left. The targets were oriented +30° upward from the projectile beam line and were connected to a high-voltage power supply to simulate spacecraft charging. The RPAs were positioned 65 and 85 mm in range at ±30° azimuth and 30° elevation from the impact point, subtending solid angles of 0.29 and 0.18 steradian, respectively. The PMT was at 110 mm range and 50° elevation from impact point (20° relative to the target normal). The patch antennas were distributed between 120 and 220 mm in range from the impact point, spanning the outward-facing hemisphere relative to the target surface.

2.2. Spacecraft Materials

The impact targets included metallic targets and representative spacecraft materials. These were arranged as shown in Fig. 2 such that each target could be translated into the projectile beam line. Two configurations each of the solar cells and OSRs were used, along with a sample of solar panel substrate. One solar cell was a LEO configuration, with uncoated coverglass. The second was a GEO configuration, which has an antireflective coating (MgF_2) and a conductive ITO (indium tin oxide) coating over the cover glass [5]. ITO is a standard transparent conductive coating composed of In_2O_3 and SnO_2. The two OSRs were both CMX glass, with composition as outlined in Tab. 1. One was a standard (uncoated) glass, while the other had an ITO coating of approximately 10 nm [6]. The solar panel substrate was composed of an aluminium honeycomb core, graphite face sheet, Kevlar (aramid fibre), and amber Kapton (polyimide), in order from innermost layer to the surface [7]. In order to fit all target configurations within the experimental chamber, 20 mm wide samples of the OSRs were placed on top of the solar cells, which were attached to the solar panel substrate. The OSRs were electrically insulated from the solar cells using Kapton tape. The aluminium honeycomb of the solar panel and the interconnects of the solar cells were connected to a current-limited high-voltage power supply to simulate spacecraft surface charging.

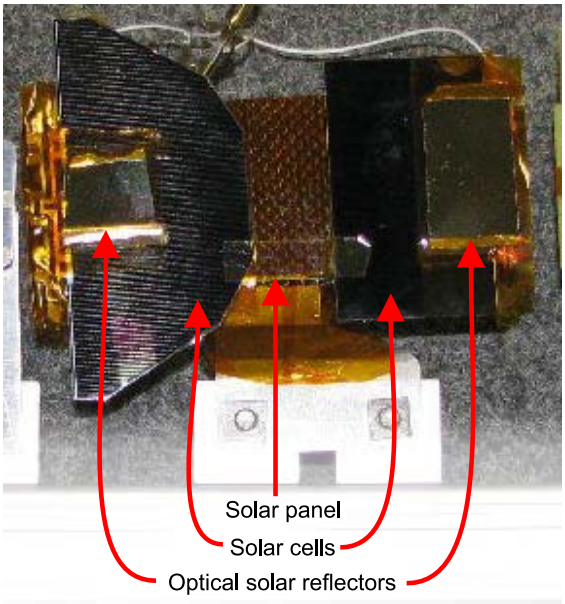

Figure 2. Photo of the spacecraft target materials used in the experimental campaign. These targets were mounted on a common frame, which could be translated horizontally within the chamber to move each target individually into the projectile beam line. From left to right, the spacecraft target materials include the standard (uncoated) OSR, LEO (uncoated) solar cell, solar panel substrate, GEO (conductive) solar cell, and conductive OSR.

Table 1. Approximate composition of the CMX glass used in the OSRs [6] and molecular weights of each constituent.

Material	Amount	Molecular weight
SiO_2	60–70%	60
Na_2O	5–10%	62
CeO_2	~ 5%	172
Al_2O_3	2–5%	102
K_2O	2–5%	94
ZnO	2–5%	81
B_2O_3	2–5%	70
CaO	< 2%	56
MgO	< 2%	40
TiO_2	< 2%	80
BaO	< 2%	153
F	< 1%	19
Sb_2O_3	< 1%	292

2.3. Observed Impacts

The results from this paper are obtained from a total of 442 impacts observed on the five spacecraft targets electrically biased to a potential of −300 V relative to the chamber ground. This bias level was selected to be representative of levels seen on orbit [5]. The impacts are broken down by target material as described in the first column of Tab. 2. This is a subset of the 6529 impact events observed through the experimental campaign, spanning additional target materials, bias levels, and sensor configurations [8] which are beyond the scope of the results presented here. Results focusing on the plasma measurements on the metallic target [9] and the patch antenna measurements [10] are published elsewhere. These prior results have shown detection of RF emission associated with certain impact configurations, and have studied in detail the behaviour of the impact plasma associated with the baseline metallic target, but thus far only a cursory examination of the impact plasmas from spacecraft targets has been performed. In the following section, we examine these five targets in detail.

3. RESULTS

Here, our results focus on determining the ion species present in the plasma formed from impacts on the spacecraft materials and on the scaling of plasma production with impact parameters. By understanding these aspects of hypervelocity impact plasma formation, we can better predict the potential threat posed by on-orbit impacts of space debris and meteoroids on spacecraft components that are represented by the materials tested in this experiment.

3.1. Ion Composition

In Fig. 3, we show representative measurements of the net plasma current detected by the RPAs. On the left are measurements of impact events at speeds representative of space debris (approximately 10 km/s) associated with each of the five spacecraft targets, and on the right are five impact events at speeds representative of meteoroids (approximately 50 km/s). The impact parameters for these events are summarised in Tab. 3. The measurement of optical flash from the PMT is used to assist in determining the time of impact for each of these individual events. Because of the −300 V bias applied to the targets, an electric field is formed between the targets and the grounded RPAs. This electric field separates the plasma species and accelerates the negatively charged plasma particles toward the sensor. Assuming singly charged species undergoing uniform acceleration without any interaction between particles, the time of flight will depend only on the mass of the particles and initial speed. This assumption is valid for determining plasma composition from the plasma current measurements [9]. For particles that are initially slow relative to the speed imparted by the electric field, the mass of the particle m can be related to the time of flight t as

$$m = \frac{qE_{\text{ext}}t^2}{2d}, \tag{1}$$

where q is the charge on the particle, E_{ext} is the external uniform electric field, and d is the distance traversed between the point of impact and the sensor.

Table 2. Breakdown of the number of impact events by target material, including the total number of impacts recorded during the experiment, the number of impacts used for the integrated RPA measurements shown in Fig. 4, and the number of impacts where an electron peak was detected as plotted in Fig. 5.

Target material	Total number of impacts	Number of impacts used for integrated measurement	Number of electron peak detections
LEO solar cell (uncoated)	52	24	30
GEO solar cell (conductive)	72	57	63
OSR (uncoated)	43	7	34
OSR (conductive)	127	108	116
Solar panel	148	33	50
Total	442	229	293

Table 3. Summary of impact parameters, including projectile mass and impact speed, for the impact events shown in Fig. 3. Note that because of the physical limitations of the electrostatic accelerator, the faster projectiles are two orders of magnitude lower in mass than the slower projectiles.

Target material	Debris speeds		Meteoroid speeds	
	Mass [fg]	Speed [km/s]	Mass [fg]	Speed [km/s]
LEO solar cell (uncoated)	30	9.5	0.36	51.1
GEO solar cell (conductive)	28	11.0	0.76	51.8
OSR (uncoated)	34	9.9	0.74	39.0
OSR (conductive)	50	9.5	0.66	51.0
Solar panel	12	12.2	0.74	53.2

The measurements plotted in Fig. 3 show that generally, the faster impacts result in a stronger plasma current, indicative of greater charge production, despite the lower projectile mass by two orders of magnitude. This is consistent with the plasma production mechanism following a power law of the form $Q \sim m^{\alpha} v^{\beta}$ with Q the charge produced, m the projectile mass, and v the impact speed, and where α is near unity and β is approximately 4, as reported in previous studies [11, 12, 13]. The particular measurements shown here for the conductive OSR target do not follow this trend, but this is attributed to the data set for this target having greater variation in signal strength throughout the projectile masses and impact speeds observed. Some of these targets show multiple peaks, indicative of different species within the impact plasma. However, the measurement noise associated with each impact event is high enough to prevent clear identification of many ion species.

In order to enhance the measurement over the sensor noise, we integrate the measurements over multiple impacts, as described in the second column of Tab. 2. These cumulative measurements are shown in Fig. 4 for each of the five targets. Here, we have used the constant acceleration assumption to convert the horizontal axis from time to atomic mass. Unfortunately, the mass resolution of the sensor configuration precludes separation of the projectile's iron ions (atomic mass of 56 amu) from the SiO_2 ions (atomic mass of 60 amu) present in the glass targets. However, the integrated measurements show that the plasma formed from impacts on the uncoated LEO solar cell includes negative ions of H^- and $Al_2O_3^-$ in addition to the peak associated with Fe^- and SiO_2^-. In contrast, the negative ion peaks associated with the conductive GEO solar cell are much smaller relative to the electron component, though the presence of $Al_2O_3^-$, Fe^-, and SiO_2^- is still evident. The uncoated OSR also shows peaks associated with $Al_2O_3^-$, Fe^-, and SiO_2^-. Additionally, the electron peak produces a positive response on the sensor rather than a negative response as with the other targets. This is an effect of secondary electron emission associated with high-energy impact of the electrons [14, 15] on the metallic collector surface of the RPA, and indicates that the energy of the electron population associated with the uncoated OSR is higher than the electrons associated with the other targets. The timing of the electron pulse is also earlier than that of the other targets, supporting the conclusion that this effect is because the electrons are higher in energy. The conductive OSR, like the conductive solar cell, show a reduced ion component relative to the electron population, but in addition to the typical $Al_2O_3^-$, Fe^-, and SiO_2^- ions present, a peak is also evident that is associated with In^- from the conductive coating. Finally, the solar panel shows only one weak negative ion peak at approximately 40 amu which may be associated with a small hydrocarbon fragment.

3.2. Electron Charge Production

In our previous work [10], we have detected strong RF emission associated with impacts on target configurations that accelerate negatively-charged species away from the target. The higher mobility of electrons in contrast to more massive ion species suggests that the RF emission is predominantly caused by the current pulse associated with the electron population. To characterise the threat of RF emission associated with this bulk electron acceleration, we measure the amplitude of the RPA measurement peak associated with electrons, for individual impact events. These results are presented in Fig. 5. Here, individual impacts are plotted by projectile mass and impact speed and colour-coded according to the voltage amplitude of the electron peak. Impacts where the peak is below the sensor noise are plotted in grey. The number of impacts with a detected electron peak are described in the third column of Tab. 2. These results show that the conductive targets in general produce stronger signal (more electrons) than the uncoated targets. However, the LEO solar cell, conductive OSR, and solar panel have many more impacts at space debris speeds without detected electron pulses in comparison to the GEO solar cell and uncoated OSR. The solar panel has the lowest level of electron production out of the five targets. The softer material of the target may reduce the total amount of plasma produced by providing a slower deceleration of the projectile as it impacts the surface, or the polymer molecular structure may be more robust to ionisation than the molecular matrix of the glass targets.

In order to provide further insight into the threat posed by space debris and meteoroids on orbit, we associate the measurements for each target with the charge pro-

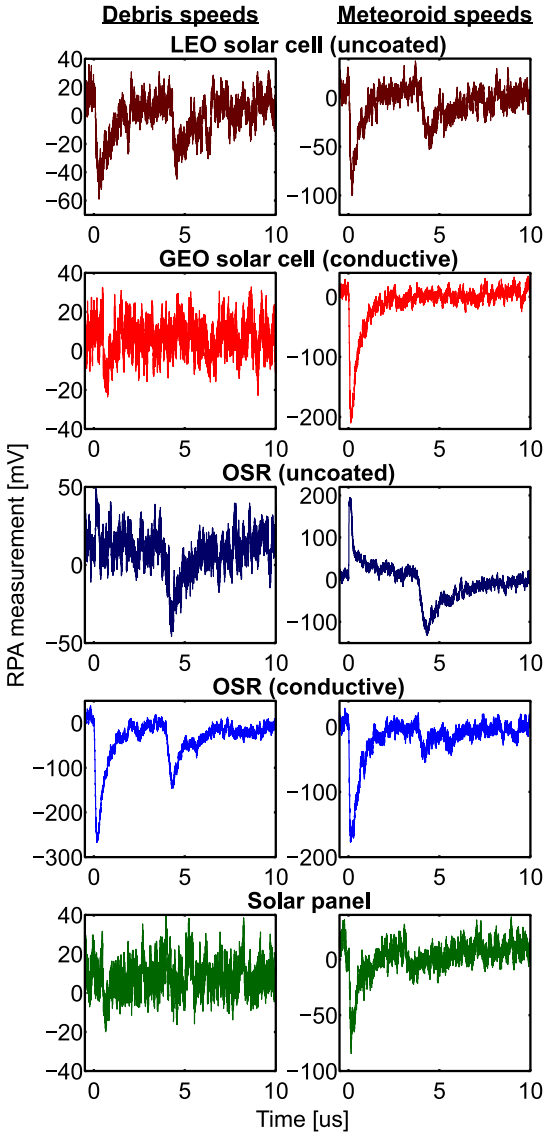

Figure 3. Measurements of net current from the plasma formed by ten individual impacts. On the left are impacts at impact speeds representative of space debris impacts. From top to bottom, these are impacts on the LEO (uncoated) solar cell, GEO (conductive) solar cell, standard (uncoated) OSR, conductive OSR, and solar panel. The projectile masses and impact speeds are summarised in Tab. 3.

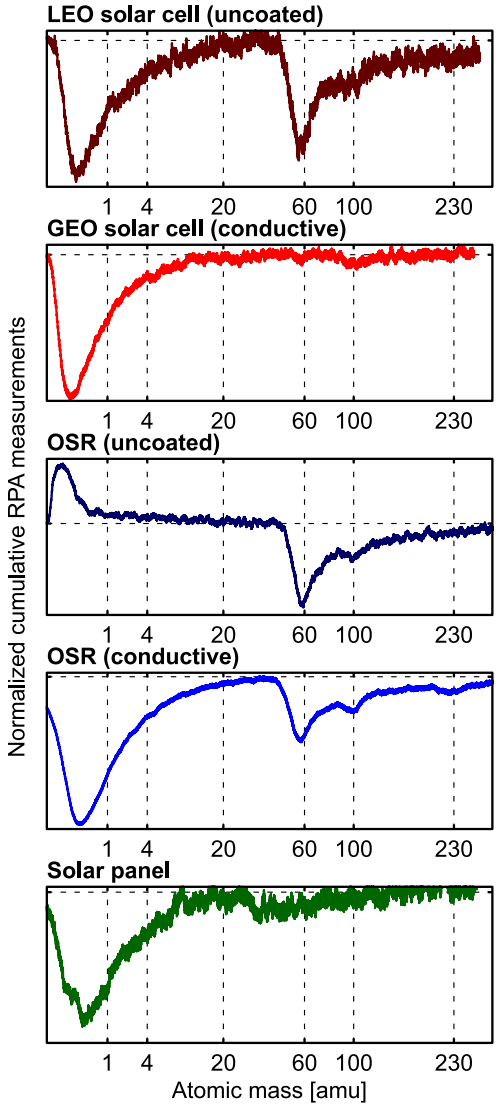

Figure 4. Integrated measurements of net current from the plasma formed by impacts on each spacecraft target. These are temporal measurements scaled using a constant acceleration assumption to indicate RPA response as a function of atomic mass of the various plasma species. A threshold on impact speed was applied for each target material to avoid misalignment uncertainties associated with the weaker signals. From top to bottom, these are measurements from impacts on the LEO (uncoated) solar cell (> 14 km/s), GEO (conductive) solar cell (> 9 km/s), standard (uncoated) OSR (> 9 km/s), conductive OSR (> 9 km/s), and solar panel (> 20 km/s).

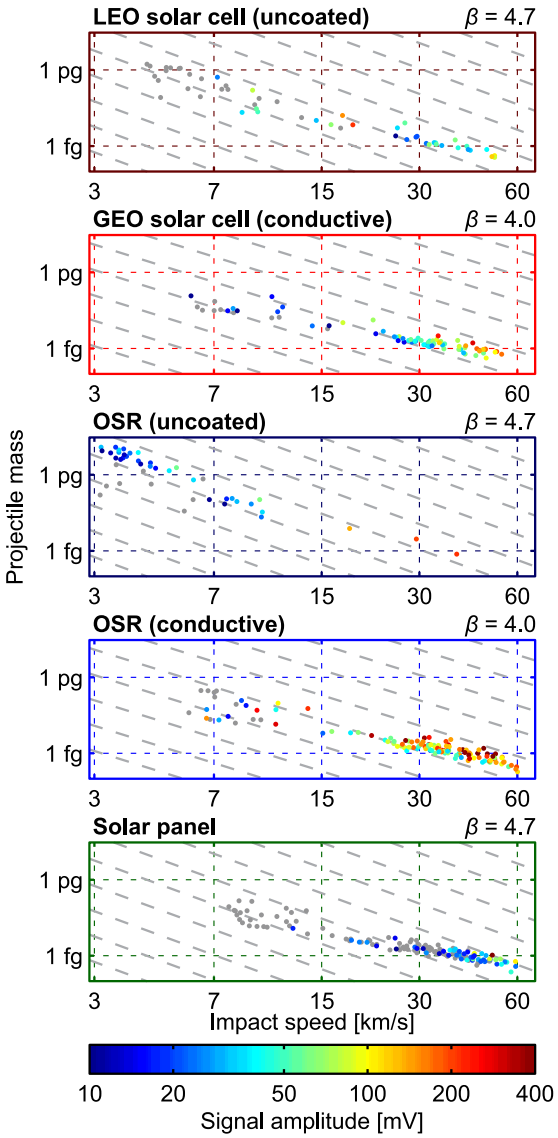

Figure 5. Electron production from impacts on each spacecraft target. Each point is an individual impact plotted by its projectile mass and impact speed, and colour-coded for the amplitude of the RPA measurement associated with the electron pulse. Impacts with no detected electron pulse are plotted in gray. From top to bottom, these are measurements from impacts on the LEO (uncoated) solar cell, GEO (conductive) solar cell, standard (uncoated) OSR, conductive OSR, and solar panel. The dashed diagonal lines represent contours of the associated power law with the slope depending on the velocity exponent β.

duction power law $Q \sim m^{\alpha} v^{\beta}$ where Q is the now the electron charge produced. We assume as before that α is unity, and vary β to fit the measurements. The contours of the power laws for each target are plotted as the diagonal dashed lines in Fig. 5. Electron production from impacts on non-conductive targets appear to follow a power law with a velocity exponent of 4.7, which is consistent with the measurements reported by Ratcliff et al. [13]. However, the conductive targets appear to follow a power law with a velocity exponent no greater than 4.0. A more definitive power law fit is difficult to achieve given the coupling of projectile mass and impact speed based on the accelerator technology.

4. CONCLUSION

From measurements of the plasma current produced by hypervelocity impacts, we find that the composition and quantity of negatively-charged constituents of the impact plasma on different spacecraft targets can vary drastically by material. Therefore, the threat of electrical anomalies on spacecraft will also be dependent on the material of the impact surface. In particular, the effect of electrical anomalies caused by electron motion will scale differently with conductive and non-conductive targets. The higher velocity exponent associated with conductive targets indicates that there will be a greater difference between the effects of meteoroid and space debris impacts on these targets, while the plasma produced by impacts on non-conductive surfaces have a lower velocity dependence. The highly energetic electron pulse associated with the uncoated OSR is particularly concerning because the faster electron speeds will be associated with stronger RF emission.

These results show that spacecraft material, in addition to surface charging and impact speed, is a strong determinant in the threat of space debris and meteoroid impacts on spacecraft electrical systems. By accounting for the distribution of materials on spacecraft surfaces, as well as spacecraft orbital conditions, the dependence of spacecraft charge on orbit altitude and orientation, and the distribution of debris in different orbits, it is possible to propose orbital configurations that minimise the threat of electrical anomalies caused by hypervelocity impact plasmas.

Future experiments are planned to study RF emission from hypervelocity impact plasmas produced at a light-gas gun facility to obtain measurements associated with larger projectiles. Furthermore, the direct effect of this phenomenon on representative electrical systems has not yet been fully understood and requires investigation at a suitable ground-based facility. Finally, we plan to obtain in situ measurements of impacts on orbit using either a hosted payload experiment on a large spacecraft or a stand-alone CubeSat mission.

ACKNOWLEDGMENTS

This study was sponsored by Los Alamos National Laboratory. The authors thank P. Colestock, S. Green, and the personnel of the Cosmic Dust Group at MPIK for their support during the experiments, J. Likar for the contribution of sample spacecraft materials, and J. Doolittle and G. King for their assistance in our plasma sensor calibration. A. Goel, T. Johnson, D. Lauben, I. Linscott, and D. Strauss also contributed to the experiment.

REFERENCES

1. Kessler, D. J. and Cour-Palais, B. G. (1978) Collision frequency of artificial satellites: The creation of a debris belt. *Journal of Geophysical Research*, **83**, 2637–2646, doi:10.1029/JA083iA06p02637.
2. Ceplecha, Z., Borovička, J., Elford, W. G., ReVelle, D. O., Hawkes, R. L., Porubčan, V. Í., and Šimek, M. (1998) Meteor phenomena and bodies. *Space Science Reviews*, **84**, 327–471, doi:10.1023/A:1005069928850.
3. Close, S., Colestock, P., Cox, L., Kelley, M., and Lee, N. (2010) Electromagnetic pulses generated by meteoroid impacts on spacecraft. *Journal of Geophysical Research*, **115**, doi:10.1029/2010JA015921.
4. Mocker, A., et al. (2011) A 2MV Van de Graaff accelerator as a tool for planetary and impact physics research. *Review of Scientific Instruments*, **82**, 095111, doi:10.1063/1.3637461.
5. Bogorad, A., Bowman, C., Herschitz, R., Krummann, W., and Hart, W. (1993) Differential charging control on solar arrays for geosynchronous spacecraft. *Nuclear Science, IEEE Transactions on*, **40**, 1542–1546, doi:10.1109/23.273507.
6. Gray, A. Email correspondence, 22 March 2013.
7. Likar, J. Email correspondence, 31 August 2011.
8. Lee, N. (2013) *Understanding Spacecraft Electrical Anomalies: Theory and Experiments Characterizing Hypervelocity Impact Plasma Dynamics*. Ph.D. thesis, Stanford University.
9. Lee, N., et al. (2013) Theory and experiments characterizing hypervelocity impact plasmas on biased spacecraft materials. *Physics of Plasmas*, **20**, 032901, doi:10.1063/1.4794331.
10. Close, S., et al. (2013) Detection of electromagnetic pulses produced by hypervelocity micro particle impact plasmas. *Physics of Plasmas*, **in review**.
11. Dietzel, H., Neukum, G., and Rauser, P. (1972) Micrometeoroid simulation studies on metal targets. *Journal of Geophysical Research*, **77**, 1375–1395.
12. McBride, N. and McDonnell, J. A. M. (1999) Meteoroid impacts on spacecraft: sporadics, streams, and the 1999 Leonids. *Planetary and Space Science*, **47**, 1005–1013.
13. Ratcliff, P. R., Burchell, M. J., Cole, M. J., Murphy, T. W., and Allahdadi, F. (1997) Experimental measurements of hypervelocity impact plasma yield and energetics. *International Journal of Impact Engineering*, **20**, 663–674, doi:10.1016/S0734-743X(97)87453-2.
14. Dekker, A. J. (1958) Secondary electron emission. Seitz, F. and Turnbull, D. (eds.), *Advances in Research and Applications*, vol. 6 of *Solid State Physics*, pp. 251 – 311, Academic Press.
15. Shih, A., Yater, J., Hor, C., and Abrams, R. (1997) Secondary electron emission studies. *Applied Surface Science*, **111**, 251–258.